RSC Advances

PAPER

View Article Online
View Journal | View Issue

Cite this: *RSC Adv.*, 2026, **16**, 2149

Toward an understanding of microalgae EPS-based selectivity and binding mechanisms for trace metal ions using Love wave acoustic and voltammetric sensors in seawater

Zouhour Mazouz, *[ab] Jihène Ammar,[a] Ollivier Tamarin,[cd] Houneida Sakly,[be] Maxence Rube,[cd] Rafik Kalfat,[f] Jean-Luc Lachaud,[cd] Corinne Dejous[cd] and Hatem Ben Ouada[a]

This study investigates the interactions between microalgal extracellular polymeric substance (EPS) and six environmentally relevant trace metals (Cu^{2+}, Pb^{2+}, Hg^{2+}, Cd^{2+}, Co^{2+}, and Ni^{2+}) in natural sea water across a concentration range from 10^{-14} to 10^{-4} M. The focus is on evaluating the functionality of EPS as a bioinspired coating layer in the development of acoustic (Love wave type Surface Acoustic Wave, SAW) and electrochemical (Square Wave Voltammetry, SWV) sensors for *in situ* trace metal monitoring in the marine environment. Fourier-transform infrared (FTIR) spectroscopy and Scanning Electron Microscopy-Energy-Dispersive X-ray Spectroscopy Analysis (SEM-EDX) confirmed successful EPS immobilization on silicon dioxide and gold surfaces, with characteristic spectral shifts indicating coordination-based interactions with target metal ions. Acoustic measurements using variations of resonance frequency and amplitude as a function of metal ion concentration showed the highest sensitivity (amplitude attenuation of 6.29 and 5.69 dB per decade) with lead and mercury. Electrochemical characterization in seawater conducted with and without redox mediators revealed metal-specific differences in peak currents, redox potentials and overpotentials. Although the high ionic strength of seawater and metal–EPS reduced direct SWV responses in some cases, the use of a ferri/ferrocyanide mediator improved the sensitivity and selectivity of detection particularly for lead (12.76 μA per decade) and mercury (12.60 μA per decade). The results demonstrate that EPS-functionalized surfaces generate a distinct mechanical and electrochemical signature for each target metal, highlighting the potential of an EPS-based bioinspired coating for developing sustainable, selective, and environmentally relevant sensing platforms for monitoring and remediating marine trace metal pollution.

Received 10th November 2025
Accepted 28th December 2025

DOI: 10.1039/d5ra08673f

rsc.li/rsc-advances

Introduction

The aquatic ecosystems are under severe threat by trace metal pollution with bio-accumulative and toxic properties comprising mercury (Hg), cadmium (Cd), lead (Pb), copper (Cu), cobalt (Co), nickel (Ni), chromium (Cr), zinc (Zn), and arsenic (As).[1–3]

According to Patil *et al.*,[4] Madhav *et al.*,[5] and Calvo-Flores *et al.*,[6] these anthropogenic contaminants inhibit the metabolic, enzymatic, and reproductive functions of marine organisms, thereby causing substantial biodiversity loss and ecological imbalance. Economically, trace metal pollution reduces fishery yield, induces constraints on aquaculture production, involves heavy expenditure for environmental monitoring and remediation, and prevents international trade in seafood.[7–10]

These environmental and economic challenges considered call for the quick development of detection and remediation technologies that are more green, sensitive, and efficient. In this regard, microalgal-derived extracellular polymeric substances (EPS) have emerged as promising biotechnological tools.

EPS appear to serve a dual function, *i.e.*, as selective biosorbents and bio-recognition layers pertaining to sensor systems.[11–15] Such biological matrices contain polysaccharides, proteins, lipids, and nucleic acids with many functional groups

[a]*Blue Biotechnology and Aquatic Bioproducts Laboratory (B3 Aqua), National Institute of Marine Sciences and Technologies (INSTM), Monastir Annex 5000, Tunisia. E-mail: mazouz.zouhour645@gmail.com*

[b]*Research Center for Microelectronics and Nanotechnology, Sousse Technopark, P. O. Box 334 Sahloul, Sousse 4054, Tunisia*

[c]*University of French Guiana, Espace-Dev, UMR 228, 97300, Cayenne, France*

[d]*Univ. Bordeaux, CNRS, Bordeaux INP, IMS, UMR 5218, Talence, F-33400, France*

[e]*RIADI Laboratory, ENSI, Manouba University, Campus Universitaire de la Manouba, La Manouba, Tunisia*

[f]*LMTA Laboratory, INRAP, BioTech Pole Sidi Thabet, Sidi Thabet 2020, Ariana, Tunisia*

like carboxyl, hydroxyl, amino, sulfate, and phosphoryl groups, providing metal binding potential through ion exchange, adsorption, and complexation.[16–19] From an environmental perspective, their natural occurrence, biodegradability, and non-toxic nature qualify them as environmental-friendly agents in sequestering metals in contaminated aquatic ecosystems. Economically, microalgae cultivation is relatively low-cost, scalable, and can be implemented along with existing wastewater treatment or aquaculture systems, thus providing additional value for the opportunity of biomass valorization. Continued research to optimize EPS production, functionalization, and application in sensors and remediation technologies gives microalgae EPS a viable sustainable remedy to the world's heavy metal pollution challenge.[20–22]

Microalgae EPS–metal interactions, that are species-specific, have been shown in many types of microalgae. Microalgal EPS carboxyl's group play vital roles in the binding of metals, most especially copper.[23,24] Protein components of EPS contribute to the sorption of cadmium and silver in *Chlorella vulgaris*, with the exception of arsenic in *Chlorella pyrenoidosa*.[25–27] EPS from *Parachlorella kessleri* and *Chlorella vulgaris* showed strong binding to cadmium and lead;[28] while in *Chlamydomonas reinhardtii*, EPS selectively enhances copper over zinc binding.[29] *Graesiella* sp. excels in Cu^{2+}, Fe^{2+}, Zn^{2+}, and Pb^{2+} metal sorption activity.[12] In addition, EPS also mitigates metal toxicity by altering speciation and reducing bioavailability.[30,31]

Recent research has demonstrated the successful application of microalgal EPS *via* self-assembled monolayers into electrochemical systems intended for detection of trace metals.[32,33] It is worth noting that EPS extracted from the thermophilic microalga *Graesiella* sp. were utilized for functionalization of electrochemical impedance spectroscopy (EIS) and surface acoustic wave (SAW) sensors. The EPS-functionalized sensors exhibited extremely high sensitivity towards cadmium (Cd^{2+}) and mercury ions (Hg^{2+}) in concentrations as low as 10^{-10} M. The EIS-based sensors demonstrated a saturation response for Cd^{2+} at 10^{-7} M, while SAW sensors displayed a larger detection range for Hg^{2+}, demonstrating the complementarity of the two modalities.[13] The most recent study was done by Gongi *et al.*[34] who used EPS sensor to evaluate both mechanical and dielectric properties of real turbid liquid solutions towards detecting mercury across very wide concentration ranges (10^{-10} to 10^{-2} M). Mechanical parameters (insertion loss and phase) were minimally influenced by water turbidity while electrical parameters (resistance and capacitance) showed a positive correlation with turbidity levels. Overall, the EPS sensors offer a robust emerging platform for simultaneous chemical and physical water quality monitoring.[35]

Recent studies emphasize the importance of microalgal EPS in the context of sensor development and multi-metal treatment. Particularly noteworthy is the application of an EPS-modified Love wave acoustic sensor in the coastal waters of French Guiana, where effective detection of mercury ions has been demonstrated in concentrations spanning 10^{-10}–10^{-2} M, even in physically turbid samples. The result clearly indicates the effectiveness of EPS modified sensors in *in situ* monitoring in marine systems.[36] Moreover, EPS-modified alginate beads in packed bed columns proved their efficiency in continuous biosorption processes in single, binary, and triple metal solutions, thus identifying the importance of EPS functionalization in real multi-metal studies.[37,38] Additionally, studies in the area of microalgal EPS composition-binding interactions in the year 2025 clearly explained the functional groups responsible for Pb(II) binding affinity to EPS, thus confirming the functionality of EPS in the identification of heavy metals through mechanistic understandings.[39,40]

.To present the sensor-based approach, it should be noted that the latest reviews and analyses emphasize the importance of biopolymer-based electrochemical sensors and nanotechnology-based platforms in the detection of trace amounts of heavy metals, thus identifying the importance of EPS in sustainable sensor platforms for efficient detection.[41,42]

Yet, in spite of the possibilities presented, EPS–metal sensorics under realistic marine conditions continue being under-investigated. As many other ions are present in seawater, these could compete for the same sites on the EPS with target metals, altered metal speciation and binding to EPS due to natural ligands, and slightly alkaline pH levels.[18,43,44] Seawater viscosity and salinity can vary in physical properties, such that if sensor efficacy is to be preserved, calibration and optimal material configurations will be required.[45–48] Seawater indeed requires sensor modification of higher order than that in fresh waters; both electrochemical and acoustic sensors require calibration based on the ionic and organic content of the particular water matrix, but the use of materials like microalgal EPS can enhance their selectivity and sensitivity in both environments, although performance may vary depending on the properties of the water.

The final objective of the current study is to investigate the binding relationships of microalga EPS with six environmentally important trace metals (Cu^{2+}, Pb^{2+}, Hg^{2+}, Cd^{2+}, Co^{2+}, Ni^{2+}) in the marine environment and will further evaluate the potential of EPS for sensitive layers in the development of acoustic (SAW) and electrochemical sensor technologies for use in marine environments. By understanding these interactions and developing them into measurable signals, it aims to advance real-time monitoring of trace metal pollution in marine ecosystems using sustainable, bio-inspired platforms.

Materials and methods

EPS solution

Cultures of the cyanobacterium *Leptolyngbya* sp. were carried out for the extraction of extracellular polymeric substances (EPS) through a tangential flow ultra filtration system (Vivaflow 50) equipped with 30 kDa pore size Millipore membranes according to Gongi *et al.*[49] The EPS-rich retentate was then washed with deionized water until conductivity stabilized, indicating the effective removal of low molecular weight compounds. The final retentate was freeze-dried and the dry mass was measured to determine the EPS yield.

For experimental use, EPS solutions were prepared by dissolving the lyophilized EPS powder in absolute ethanol (99% purity; Sigma-Aldrich) at a concentration of 1 mg mL^{-1}. The

solution was vortexed and then filtered through a 0.2 μm syringe filter (Sartorius, Bohemia, New York, USA) to remove any insoluble residues, following the procedure described by Gongi *et al.*[12]

The reproducibility of EPS batches was verified through FTIR spectroscopy, which showed consistent functional group profiles across extractions, confirming chemical identity without significant variability.[50]

Metal solutions

Six divalent metal ions of Pb^{2+}, Hg^{2+}, Cd^{2+}, Cu^{2+}, Co^{2+}, and Ni^{2+} were examined in this study. Stock solutions of each metal were prepared by dissolving their respective high-purity nitrate salts in natural seawater. The metal salts used were: lead(II) nitrate (99%), mercury(II) nitrate dihydrate (98%), cadmium nitrate tetrahydrate (≥99%), copper(II) nitrate trihydrate (99%), cobalt(II) nitrate hexahydrate (98%), and nickel(II) nitrate hexahydrate (99.9%). All chemicals were sourced from Thermo Fisher Scientific.

Natural seawater was collected directly from the sea and filtered through a 0.2 μm membrane filter (Sartorius, Bohemia, New York, USA) to remove large particulates and suspended solids. The filtered seawater was then adjusted to pH 5.2 by addition of a commercial 3 M sodium acetate buffer solution to achieve a final buffer concentration of 0.1 M, thereby stabilizing the ionic environment and ensuring reproducible conditions for the subsequent electrochemical (voltammetric) and acoustic (Love-wave) measurements. The $[Fe(CN)_6]^{3-/4-}$ redox couple was employed as a mediator in the electrochemical voltammetric measurements to facilitate electron transfer and enhance signal detection.

To obtain a range of metal ion concentrations, serial dilutions were carried out, producing aqueous solutions with concentrations ranging from 10^{-14} M to 10^{-2} M. All glassware used in the preparation of solutions was thoroughly acid-washed with 10% nitric acid and rinsed with deionized water to prevent metal adsorption and contamination.

For comparison, deionized freshwater metal solutions were also prepared using the same procedure.

Natural seawater introduces complications because of its variable ionic strength and dissolved organic matter. We controlled these variables through appropriate experimental design choices. For instance, the samples were dosed with sodium acetate buffer to a final concentration of 0.1 M at pH 5.2 to define a stable ionic background that offsets natural salinity changes. This is a strategy commonly applied in environmental electrochemistry to ensure the observed current responses depend on the buffer composition rather than fluctuating marine conditions.[51] Similarly, acoustic measurements benefited from this same type of strategy: a dual delay-line configuration is used with an uncoated reference channel to subtract the background signals from properties in bulk seawater (*e.g.*, conductivity, viscosity, temperature). A differential approach isolates signals arising specifically from EPS–metal interactions. Dissolved organic matter was treated by baseline measurements: we recorded blank voltammograms in seawater in advance of metal addition in electrochemical work and subtracted them from the signal measured in the presence of metal; in acoustic work, we allowed the sensor baseline to equilibrate in seawater before data collection. Thus, these methods-buffering, filtration, differential measurement, and baseline subtraction-are combined in order to control for matrix effects and ensure that signals reported originate from specific binding of metals to EPS.[52]

Acoustic sensor preparation and detection

Love wave acoustic sensors were fabricated on 500 μm-thick AT-cut piezoelectric quartz substrates with silica (SiO_2) waveguiding layers deposited by Plasma-Enhanced Chemical Vapor Deposition.[53,54] The devices incorporated dual delay-line architecture, each featuring gold–titanium interdigitated transducers (IDTs) for surface acoustic wave generation and detection, with one delay line serving as the active sensing channel and the other as an environmental reference.

Sensor functionalization was achieved by depositing 80 μL of EPS solution (1 mg mL^{-1} in ethanol) into a microfluidic chamber localizing the fluid onto the acoustic path between the IDTs,[55] followed by 24-hour drying at ambient temperature to form a uniform thin film on the active sensor surface.

Metal detection was conducted by introducing 30 μL of metal salt solutions in increasing concentrations, recording stabilized acoustic signals at each step, and ensuring careful sample handling to prevent membrane damage or contamination. The sensor electrical characterization was carried out by measuring the scattering parameter in transmission (S_{21}) with a Vector Network Analyzer (NanoVNA-F V2, https://www.sysjoint.com/).

Electrochemical setup and measurements

The electrochemical system is based on screen-printed gold electrodes (SPGEs) (Metrohm DropSens DRP-250AT) made of a single gold (Au) working electrode (WE) 0.40 cm in diameter, centrally located on a ceramic substrate measuring 3.38 cm in length, 1.02 cm in width and 0.05 cm in thickness, and paired with a platinum (Pt) auxiliary electrode and a silver (Ag) reference electrode.

Electrochemical experiments utilized an EmStat4R potentiostat (PalmSens) with PSTrace software. Square wave voltammetry (SWV) was performed with a 10 mV amplitude, 10 mV step potential, 2 s quiet time, 17 Hz frequency, and a potential range of −0.8 to +0.8 V (*vs.* Ag pseudo-reference) at a 0.1 V s^{-1} scan rate for electrode cleaning and characterization. All experiments were conducted in triplicate ($n = 3$) at 23 ± 1 °C.

Prior to functionalization, the SPGEs underwent electrochemical cleaning *via* cyclic voltammetry (CV) in 0.1 M H_2SO_4, with 10 cycles from −0.4 V to +1.4 V (*vs.* Ag pseudo-reference) at 0.1 V s^{-1} scan rate. The electrochemical kinetics reactions were modeled using the Butler–Volmer equation,[56] eqn (1).

$$j = j_0\{\exp^{[(1-\alpha)\times z\times F\times \eta/(R\times T)]} - \exp^{[-\alpha\times z\times F\times \eta/(R\times T)]}\} \quad (1)$$

where, j is the current density (A cm^{-2}), j_0 is the exchange current density (A cm^{-2}), α is the charge transfer coefficient, z is the number of electrons transferred, F is the Faraday constant

(96 485 C mol^{-1}), η is the overpotential (V), R is the ideal gas constant (8.314 J mol^{-1} K^{-1}), and T is the absolute temperature (K).

Surface concentrations (C) related to peak currents (I_p) were estimated using the modified Randles–Sevcik equation, adapted for SWV,[45] eqn (2).

$$I_p = (2.69 \times 10^5) \times n^{3/2} \times A \times D^{1/2} \times C \times v^{1/2} \quad (2)$$

where, I_p is the peak current (A), (2.69×10^5) corresponds to the Randles–Sevcik constant at 25 °C (C mol^{-1} V$^{-1/2}$), n is the total number of electrons transferred in the overall reaction, A is the electrode area (cm^2), D is the diffusion coefficient (cm^2 s^{-1}), C is the bulk concentration (mol cm^{-3} or M) and likely represents the effective EPS pre-concentration, v is the scan rate (V s^{-1}).

Fourier transform infrared (FTIR) spectroscopy

FT-IR spectra were acquired using a PerkinElmer System 2000 spectrometer equipped with a deuterated triglycine sulfate (DTGS) detector. Measurements were performed in transmission mode using KRS-5 (thallium bromoiodide) crystal plates, with a spectral range of 4000–400 cm^{-1}, a resolution of 2 cm^{-1} and a scan speed of 2 cm s^{-1}.

Prior to sample analysis, a background spectrum was recorded in ambient air to account for atmospheric interference from water vapor and carbon dioxide. All sample spectra were subsequently normalized to this background for baseline correction.

Scanning electron microscopy and energy-dispersive X-ray spectroscopy analysis

The surface morphology and elemental composition of EPS-functionalized SAW sensors were analyzed using a Thermo Scientific Apreo S Scanning Electron Microscope (SEM) (FEI, Thermo Fisher Scientific) equipped with a Schottky Field Emission Gun, providing a resolution of 0.8 nm at 15 kV. The system included in-lens and backscatter detectors, coupled with Energy-Dispersive X-ray Spectroscopy (EDS) for quantitative elemental mapping of Cd^{2+}, Co^{2+}, Cu^{2+}, Hg^{2+}, Ni^{2+} and Pb^{2+}.

Surface roughness parameters, including arithmetic average roughness (R_a), root mean square roughness (R_q), maximum height of the profile (R_z), and total height of the profile (R_t), were evaluated to characterize the surface topography. Automated imaging and elemental analysis were performed using ChemiSEM and Maps software.

This study did not involve human participants, animals, or clinical trials; thus, ethics approval, consent to participate/publish, and clinical trial registration are not applicable.

Results and discussion

Fourier-transform infrared (FTIR) spectroscopy analysis

Fourier-transform infrared (FTIR) spectroscopy (Fig. 1a and b) confirmed the successful EPS coating and demonstrated the formation of multiple hydrogen bonds or coordination interactions with both silicon oxide (SiO_2) and gold surfaces of sensors. On SiO_2 (Fig. 1a), characteristic spectral modifications were observed that confirmed EPS attachment. The broad O–H stretching band around 3300 cm^{-1} typically intensified and shifted due to hydrogen bonding between EPS hydroxyl/carboxyl groups and surface silanols (Si–OH).

New absorption bands appeared between 2800–3000 cm^{-1} (C–H stretching), 1600–1650 cm^{-1} (C=O stretching), 1400–1450 cm^{-1} (COO^- symmetric deformation), and 1200–1260 cm^{-1} (S=O stretching), all characteristic of EPS components[39,57] and absent in pure SiO_2. The glycosidic vibrations of C–O–C and C–O around 1000–1150 cm^{-1} often overlapped or masked by the native Si–O–Si band of silica. Additionally, the

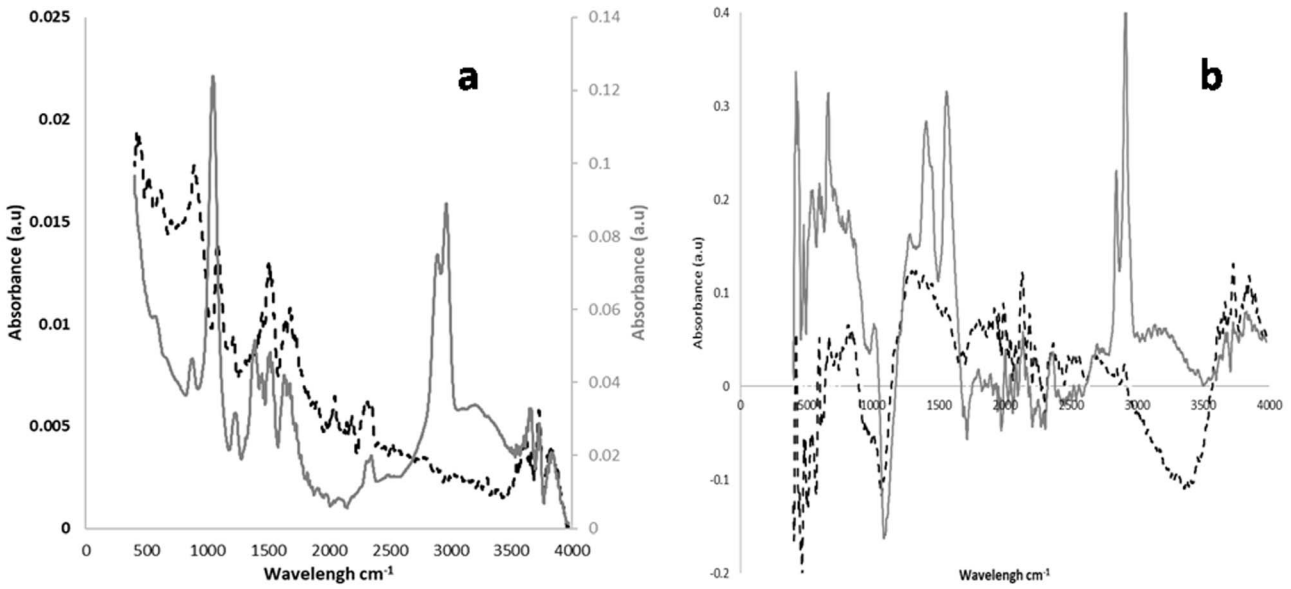

Fig. 1 FTIR spectra of EPS adsorption on (a) silicon oxide (SiO_2) and (b) gold surface sensor. Bare surface (dashed line) *versus* EPS-coated surface (solid line).

hydration capability of EPS enhanced water-related bands (H–O–H bending at ~1640 cm^{-1}).

Unlike oxide surfaces, gold does not form covalent bonds with EPS under mild conditions, but surface-enhanced IR absorption (SEIRA) effects may amplify specific vibrational modes, especially in nanoscale systems.[58,59] While gold itself lacks IR activity (Fig. 1b), EPS coating induced visible spectral bands typical of uronic acids and glycosidic structures, alongside redshifted O–H bands and intensified amide and sulfate features.[60] New bands below 900 cm^{-1}, characteristic of out-of-plane vibrations, suggest possible metal–oxygen bonding.[61] These consistent FTIR spectra across EPSs underpin the reproducibility of our extraction protocol and are in keeping with recent characterizations where FTIR, often supplemented with TOC/TN, assures chemical identity for metal-binding applications.[62–64]

Upon exposure of the sensitive EPS–SiO_2 layer to metal salts in seawater medium, FTIR spectra (Fig. 2) reveal distinct structural and spectral modifications, such as: (i) band shifts to lower wave numbers (red shift), (ii) intensity variations either increase or decrease depending on the degree of complexation and local disruption, (iii) band broadening due to hydrogen bond perturbation or chemical environment alteration, and (iv) emergence of new bands corresponding to new vibrational modes, such as metal–oxygen bond formation.

However, significant differences were observed between metals studied. O–H stretching bands (3300 cm^{-1}) exhibited shifts or broadening for nearly all studied metals, indicating coordination. C–H stretching bands (2800–3000 cm^{-1}) were less affected, as they are not directly involved in coordination, although a slight decrease in intensity is often noted due to structural rearrangement. The carboxyl/amide region (1600–1400 cm^{-1}) often shifts to lower frequencies (*e.g.*, to 1580 cm^{-1} for Hg^{2+}) and showed intensity increases (Hg^{2+}) or decreases (Cu^{2+}, Pb^{2+}). Sulfate groups (1200–1270 cm^{-1}), being highly accessible anionic sites, were notably responsive in the presence of Cu^{2+}, Hg^{2+}, and Co^{2+} ions. Glycosidic bridge regions (C–O–C, 1000–1100 cm^{-1}) experienced perturbations due to interactions involving oxygen donors, particularly with Cu^{2+} and Pb^{2+}. Additionally, new bands in the region below 900 cm^{-1} indicative of out-of-plane C–H bending appeared in cases of Pb^{2+} and Co^{2+}, suggesting potential metal–oxygen bonding vibrations.[61]

Peak intensities of key functional group bands were quantitatively studied to understand the EPS and metal binding mechanisms for each metal in relation to the uncomplexed EPS spectrum. The maximum intensity of each functional group band in the EPS with the metal was divided by the maximum intensity in the EPS alone to provide a quantitative estimate of the binding interaction for each functional group. A ratio greater than 1 indicates an increase in the intensity of the functional group band in the metal–bound EPS, suggesting coordination of the functional group to the metal. Conversely, a ratio less than 1 indicates a decrease in the intensity of the functional group band in the metal–bound EPS, reflecting inhibition of the vibrational activity of the functional group due to the binding interaction. Distinctive metal-specific binding patterns are evident from the results summarized in Table 1. For example, Cu^{2+} significantly enhances almost all functional group bands, increasing the S=O stretching band (1200–1270 cm^{-1}) of sulfated polysaccharides by more than 20-fold. This high S=O ratio clearly indicates that sulfated polysaccharide moieties are a major binding component for copper. Additionally, Cu^{2+} markedly enhances the intensity of bands corresponding to O–H (hydroxyl), C=O/amide I (protein/uronic acid carbonyl), COO^- (carboxylate), and C–O–C (glycosidic) groups, demonstrating its interaction with various EPS functional groups.

Other metals, however, exhibit more selective preferences: Hg^{2+} and Co^{2+} show their largest increases in the S=O band with ratios of approximately 2.5, also increasing the C=O/amide I region, where Hg^{2+} shows a ~2.4-fold increase. This suggests that their focus is on sulfated polysaccharides and protein/uronic acid groups. The largest intensity changes for Pb^{2+} and Ni^{2+} occur in the low-frequency metal–O region, characterized by a new band below 900 cm^{-1}, corresponding to the vibrations of the metal–oxygen bonds. These metals also show significant increases in the S=O band, indicating that they coordinate primarily through direct metal–oxygen bonds and sulfate groups. In contrast, Cd^{2+} does not result in any significant enhancement in FTIR bands (all ratios <1.0), which corresponds to the very weak binding affinity identified in our electrochemical and acoustic measurements. This quantitative FTIR analysis aligns with previous studies on EPS–metal complexes that employed spectral deconvolution and multivariate analyses to distinguish between polysaccharide and protein contributions to metal binding.[65–67]

Heavy metal complexation with EPS occurs primarily through two mechanisms: electrostatic attraction between negatively charged EPS groups and metal cations, and coordination, involving lone-pair electrons from oxygen atoms interacting with metal ions.[25,68] The strength of these interactions depends on the metal's valency and ionic radius—metals such as Cu^{2+} and Hg^{2+}, with higher charge densities and smaller ionic radii, tend to form stronger complexes.[69] In marine environments, specific physicochemical conditions further modulate these interactions. High salinity and the abundance of competing cations (Na^+, Mg^{2+}, Ca^{2+}) create a charge screening effect, reducing the electrostatic attraction between EPS and metal ions.[70] Additionally, heavy metals may form soluble complexes with marine anions (*e.g.*, $Hg^{2+} + Cl^- \rightarrow HgCl_2$), thus lowering their free ion concentration and bioavailability.[71] Moreover, EPS conformation in seawater is affected by ionic strength, potentially leading to rearrangements in the polysaccharide matrix. This can expose or shield specific binding sites.[72,73]

Scanning electron microscopy analysis

Fig. 3 presents the angular spectrum data likely obtained through SEM. This type of analysis is crucial for investigating material properties.[74] It shows the angular dependence of scattering intensity ($W_a \times 10^{-3}$ arbitrary units) as a function of angle (alpha, in degrees) for different surface conditions.

The angular spectrum revealed two main scattering directions for both bare gold and EPS-coated surfaces, with peaks around 100° and 290°. Although the scattering angles remained

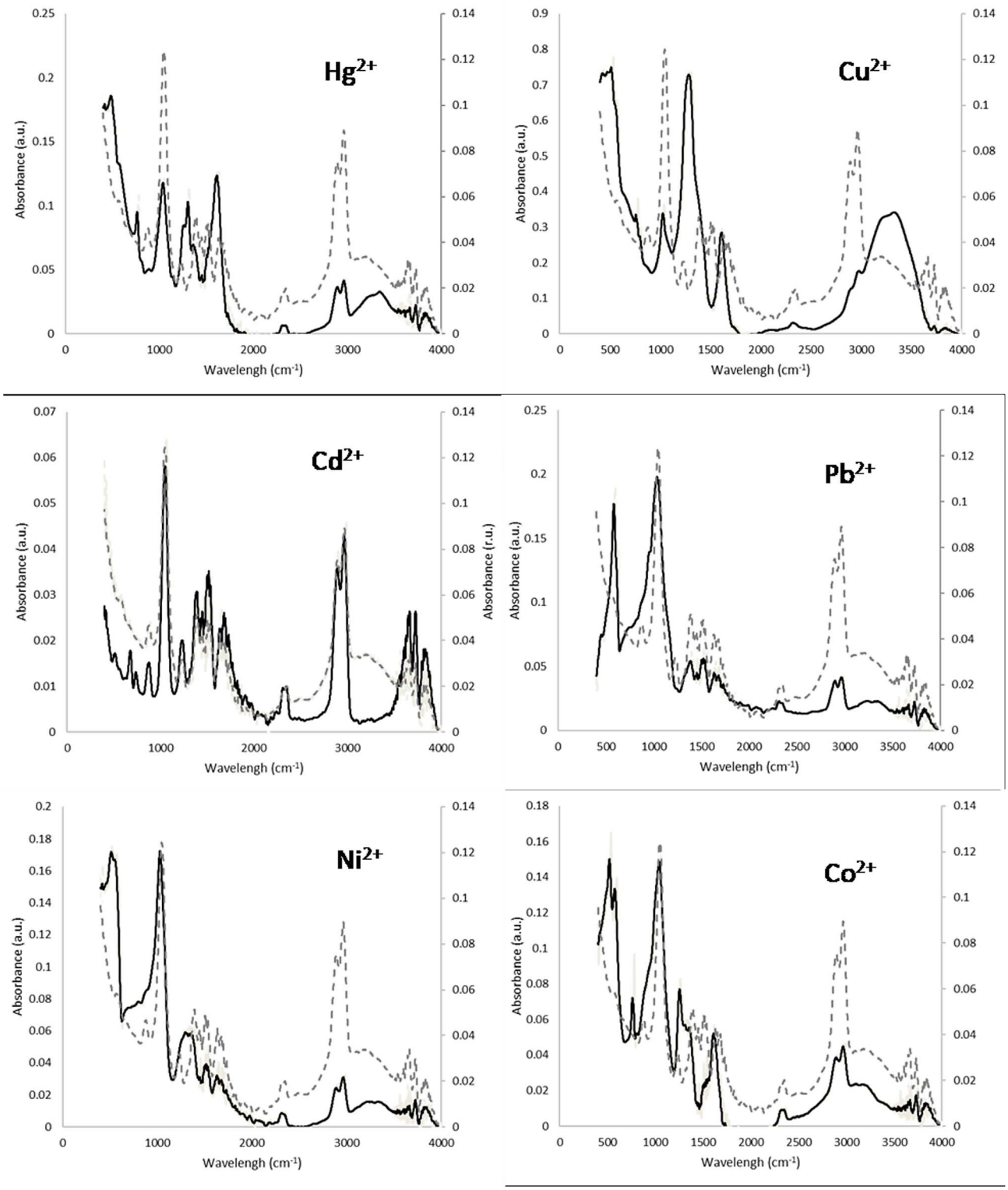

Fig. 2 FTIR spectra of EPS–SiO_2 layer in seawater exposed to metal salts (Hg^{2+}, Cu^{2+}, Cd^{2+}, Pb^{2+}, Ni^{2+}, Co^{2+}): EPS layer (dashed line, secondary axis) *versus* metal complexation (solid line).

unchanged after EPS layer deposition, the signal intensity increased significantly more than three-fold compared to bare gold. This increase suggests that the EPS layer interacts more actively with the electron beam, likely due to its higher electron density or enhanced signal response. Overall, the EPS does not alter the scattering direction but significantly enhances the scattering intensity, demonstrating effective surface coating and enhancement.

When the EPS-coated surface was exposed to different heavy metals (Cu^{2+}, Hg^{2+}, Pb^{2+}, Ni^{2+}, Cd^{2+}, and Co^{2+}), all metals

Table 1 Summary of dominant EPS functional groups in metal binding based on peak intensity ratios

Metal ion	Dominant functional groups (peak intensity ratio)
Cu^{2+}	S═O stretching (20.66), O–H stretching (10.01), COO^- symmetric (6.83), metal–O bonding (6.23), C═O/amide I (5.54)
Hg^{2+}	S═O stretching (2.68), C═O/amide I (2.39)
Co^{2+}	S═O stretching (2.49), metal–O bonding (1.58)
Pb^{2+}	Metal–O bonding (2.15), S═O stretching (1.75), C–O–C glycosidic (1.56)
Ni^{2+}	Metal–O bonding (1.78), S═O stretching (1.64)
Cd^{2+}	No strong interactions observed (all ratios <1.5)

exhibited a clear bimodal scattering pattern, with two peaks of equal intensity. This symmetry suggests that the metals interact in a balanced way across the surface. However, the angles at which these peaks occurred varied between metals, showing that each one binds or organizes slightly differently on the EPS layer. Copper, for example, exhibited strong, well-defined peaks, indicating tight binding or high surface coverage, while mercury showed weaker peaks, pointing to a less intense interaction. Cadmium displayed a unique pattern, with peaks at the beginning and middle of the angular range, suggesting different spatial organization. Lead and cobalt had very similar profiles, with peaks at the same angles and similar intensities, which likely reflects a more uniform and evenly distributed interaction. Interestingly, only Cu^{2+}, Hg^{2+}, Ni^{2+}, and Cd^{2+} produced additional scattering signals at high angles (320–350°) a feature completely absent in both the bare gold and EPS-only surfaces, as well as in the presence of Pb^{2+} and Co^{2+}. This suggests that some metals create localized changes or clustering on the surface, while others remain more evenly distributed.[75,76]

These differences in angular behavior are corroborated by SEM surface roughness data (Table 2), which provide a clearer understanding of surface changes after metal exposure.

The bare gold surface was extremely smooth, with a very low R_a value of about $(0.044 \pm 0.003) \times 10^{-3}$ μm. After EPS was added, the surface became noticeably rougher ($R_a = 0.118 \pm 0.023$ μm), reflecting the presence of a textured biopolymer layer. When metals were introduced, the roughness increased further particularly with Pb^{2+} ($R_a = 0.182 \pm 0.027$ μm) and Cu^{2+} ($R_a = 0.156 \pm 0.023$ μm), consistent with stronger surface interactions and possibly rearrangements of the EPS structure. Conversely, Hg^{2+} and Co^{2+} resulted in relatively low roughness values, in line with their smoother and more symmetric scattering profiles. The same trends were observed across other roughness parameters (R_q, R_z, R_t), confirming that each metal interacts with the EPS layer in a distinct manner, influencing both microscopic surface morphology and directional energy scattering.

Acoustic detection using SAW sensors

The differential architecture of the dual delay-line setup, with EPS being selectively functionalized only on the sensing channel, together with trace level spiking into unaltered natural seawater, guarantees full common-mode rejection of bulk seawater effects on major ions, conductivity, viscosity, density, and hence attributes the concentration-dependent phase and amplitude changes observed to specific EPS–trace metal interactions.

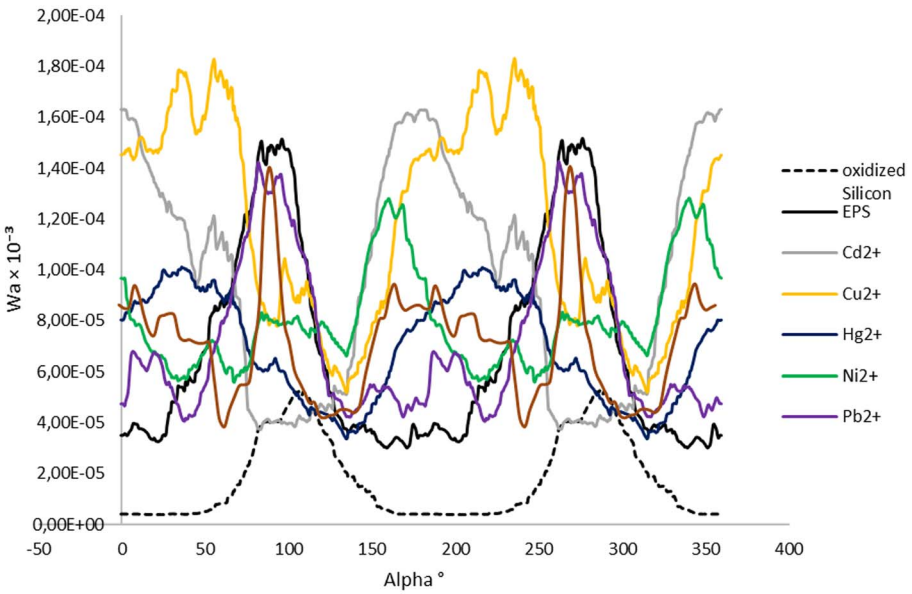

Fig. 3 Angular-resolved EDS spectra comparing alongside silicon oxide (SiO_2) substrate (black dotted line), EPS control (black line), EPS-coated sensors after exposure to Cd^{2+} (gray), Cu^{2+} (yellow), Hg^{2+} (blue), Ni^{2+} (green), Pb^{2+} (purple), and Co^{2+} (brown).

Table 2 Surface roughness parameters (μm): arithmetic average roughness (R_a), root mean square roughness (R_q), maximum height of the profile (R_z), and total height of the profile (R_t), of bare gold and EPS-coated surface of sensors with metal ions exposure. Each value represents average of three replicates

	R_a	R_q (RMS)	R_z	R_t
Bare	$(0.044 \pm 0.003)10^{-3}$	0.079 ± 0.009	0.233 ± 0.048	0.686 ± 0.188
EPS	0.118 ± 0.023	0.155 ± 0.027	0.511 ± 0.067	0.802 ± 0.047
Hg^{2+}	0.113 ± 0.024	0.152 ± 0.027	0.526 ± 0.092	0.794 ± 0.063
Pb^{2+}	0.182 ± 0.027	0.229 ± 0.026	0.731 ± 0.059	0.867 ± 0.029
Cd^{2+}	0.123 ± 0.036	0.162 ± 0.040	0.577 ± 0.117	0.820 ± 0.103
Cu^{2+}	0.156 ± 0.023	0.195 ± 0.027	0.623 ± 0.069	0.867 ± 0.057
Ni^{2+}	0.123 ± 0.024	0.162 ± 0.028	0.690 ± 0.105	0.902 ± 0.071
Co^{2+}	0.118 ± 0.018	0.157 ± 0.023	0.671 ± 0.066	0.911 ± 0.050

SAW sensors exploit acoustic waves propagating on the surface of piezoelectric materials. When a sensitive layer, such as an EPS biofilm, interacts with trace metals, changes in mass and stiffness occur that affect the velocity and amplitude of the acoustic waves. These variations can be correlated with the concentration and type of adsorbed metal.

Although the use of SAW sensors to detect microalgal EPS–metal interactions is still being explored, previous studies have demonstrated their effectiveness in detecting heavy metals in freshwater environments.[13,34] In the present study, the acoustic signal loss levels caused by the bare sensor (ranging from 30 to 32 dB) and after the deposition of the EPS layer (ranging from 35 to 36 dB), as well as the maximum frequency (119 MHz), were consistent regardless of whether the medium was seawater or deionized freshwater (Table 3).

``However, the gain curve (Fig. 4) as a function of frequency typically appeared smooth in freshwater, reflecting stable acoustic propagation conditions, while in seawater, the gain curve often became noisy, especially in the presence of trace metals. This behavior is attributed to several factors inherent to seawater. First, its high ionic strength and conductivity due to abundant ions such as Na^+, Cl^-, Mg^{2+}, and Ca^{2+} can induce electromagnetic damping and interfere with the piezoelectric substrate's wave transmission, leading to attenuation and irregularities in the signal.[77]

Moreover, the complexation of trace metals with natural organic matter and EPS in seawater modifies the dielectric properties of the interface, affecting both wave velocity and amplitude.[78,79] Seawater also increases acoustic damping due to its higher viscosity and density compared to freshwater, which alters the mass loading effects on the sensitive EPS layer. Additionally, the presence of metals like Pb^{2+}, Cu^{2+}, and Hg^{2+} leads to metal–EPS complexation and aggregation phenomena that may produce non-uniform mass deposition on the sensor surface, further contributing to signal noise.[13]

To quantify the performance comparison between the two media, we measured the acoustic signal-to-noise ratio of the EPS-coated SAW sensor in deionized freshwater *versus* natural seawater. Results, as exhibited in Table 4, show a dramatic difference between the two media. Freshwater gave an SNR of +2.53 dB for a signal-to-noise amplitude ratio of 1.338, while seawater yielded an SNR of −21.29 dB for a ratio of only 0.086. This 23.8 dB drop evidences a severe deterioration in measurement quality. Accordingly, Table 3 shows that the baseline noise rose from 0.0036 for freshwater to 0.0047 for seawater, which corroborates the increased noise floor for the marine environment. These results constitute strict justification for qualitative observations of smooth gain curves in freshwater (Fig. 4a) *versus* significant irregularities in seawater (Fig. 4b).[80–82]

Despite this signal disruption, the exposure of the six experimental metals to the sensor across varying concentrations in seawater resulted in a significant loss of the acoustic signal correlated with the type of metal (Fig. 5 and Table 3).

Cobalt showed an initial signal loss of 1.70 dB at ultra-low concentrations (10^{-14} M), which is relatively moderate compared to the other metals, and a saturation concentration of 10^{-9} M. Its saturation loss of 17.31 dB and gradient of 3.12 dB per decade of metal concentration suggest a moderate increase in signal loss as concentration increases. Nickel, conversely, exhibited the lowest initial loss at 0.22 dB, indicating a weaker response at low concentrations. However, it had the lowest saturation concentration at 10^{-12} M, reflecting rapid onset of saturation and a modest saturate loss of 3.48 dB, with a gradient of 1.63 dB per decade, indicating a relatively slow rate of signal change with increasing concentration.

Cadmium showed a stronger initial response with a signal loss of 3.60 dB at low concentrations, and it reached saturation at a similar concentration to Co^{2+} (10^{-9} M). It also demonstrates a high saturation loss of 24.14 dB, with a gradient of 4.11 dB per decade, suggesting relatively rapid signal increase with concentration.

Mercury behaved similarly to Cd^{2+}, with an initial loss of 6.58 dB, saturating at 10^{-11} M, and a saturate loss of 23.65 dB. Its

Table 3 Average loss of acoustic signal in deionized water and natural seawater. Values represent the average of six replicates. STD: standard deviation

	Bare fresh water	Bare sea water	EPS fresh water	EPS sea water
Average loss (dB)	30.10	32.70	35.99	37.13
STD	2.04	2.62	2.23	1.18

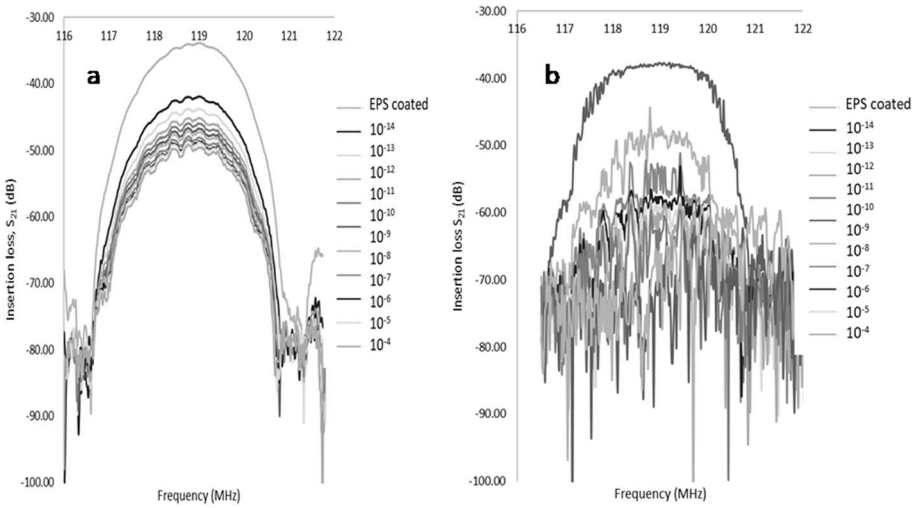

Fig. 4 Acoustic insertion loss (S_{21} parameter) *versus* frequency in (a) deionized water and (b) natural seawater for EPS-functionalized sensors exposed to varying concentrations of Hg^{2+} across the range 10^{-14} to 10^{-4} M. The concentration-dependent shift in insertion loss demonstrates the sensor's sensitivity to metal binding. Each curve represents a different metal ion concentration (M).

gradient of 5.69 dB per decade showed a very steep rate of change. Lead response was exceptional, having the highest initial signal loss of 12.65 dB, and the steepest gradient of 6.29 dB per decade. It had a saturate loss of 25.24 dB and reached saturation at a concentration of 10^{-12} M due to its high sensitivity and strong response to concentration changes. Finally, copper showed an initial loss of 4.41 dB at saturation concentration of 10^{-8} M, indicating that saturation occurs later compared to the other metals. Its saturation loss was the highest at 25.30 dB, with a gradient of 3.48 dB per decade, suggesting a less rapid but significant increase in signal loss as concentration increases.

To attribute the Love-wave sensor signals to EPS-mediated trace metal binding, as opposed to non specific interference from major seawater cations (Na^+ ~480 mM, Mg^{2+} ~54 mM, Ca^{2+} ~10 mM), we pursued a three-pronged experimental approach. First, our dual delay-line architecture with selective EPS functionalization acts as a built-in control. One sensing channel is coated with EPS, while an identical reference channel on the same substrate remains bare. Both channels are exposed to the exact same seawater matrix and metal solutions simultaneously. This design effectively cancels out all bulk matrix effects ionic strength, conductivity, viscosity, density, temperature fluctuations, and nonspecific cation adsorption by treating them as common-mode signals that are electronically subtracted in the differential measurement (Δphase and Δinsertion loss *via* S_{21} parameters). What remains is only the specific signal arising from metals interacting with the viscoelastic and dielectric properties of the EPS layer. Second, we used an ultra-wide concentration range, 10^{-14} to 10^{-4} M, which was 8–12 orders of magnitude lower than the levels of major cations in seawater. As such, the bulk ionic strength hardly changes as we titrate metals, which means that any change in conductivity or electrokinetic effects due to Na^+, Mg^{2+}, or Ca^{2+} itself cannot confound the results. Third, the metal selectivity itself provides the strongest evidence. Indeed, the acoustic signatures of the six metals produced were strikingly different; the Pb^{2+} ion had the steepest gradient, 6.29 dB per decade, followed by Hg^{2+}, 5.69 dB per decade, while Ni^{2+} was practically silent, only 1.63 dB per decade. Large variation also occurred in their saturation concentrations from 10^{-12} to 10^{-9} M (Table 5 and Fig. 5). Such metal-specific "fingerprint" properties are fundamentally incompatible with non-selective matrix noise that would uniformly dampen all analytes. These diverging patterns mean that each metal binds to EPS in its own characteristic way.

The selectivity coefficients were calculated by the Separate Solution Method, SSM,[83,84] in order to establish the sensor capability to discriminate among the various trace metals studied. These coefficients, which are defined as the ratio of the sensitivity gradients of the interfering ion, j, to the primary target ion i, have been calculated from the data given in Table 5. The results are listed in Table 6. It follows that the acoustic

Table 4 Signal-to-noise ratio (SNR) analysis for Love-wave acoustic measurements in deionized freshwater and natural seawater. Baseline noise is defined as the standard deviation (SD) of background amplitude in the absence of analyte; signal is the mean amplitude during metal detection. SNR values are calculated using $SNR_{dB} = 20 \log_{10}(S/N)$

Matrix	Mean signal (dB)	Noise (SD of background amplitude)	Signal/noise ratio (amplitude)	Signal/noise ratio (dB)
Sea water	−71.70	0.0047	0.086	−21.29
Fresh water	−68.19	0.0036	1.338	2.53

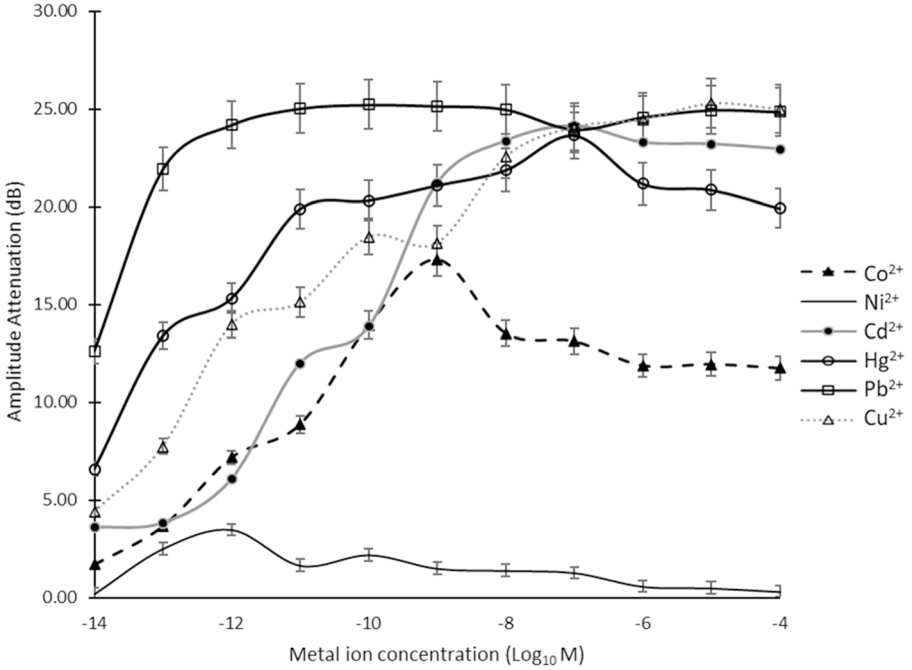

Fig. 5 Variation of acoustic insertion loss (amplitude attenuation) as a function of metal ion concentration in natural seawater for six trace metals (Pb^{2+}, Hg^{2+},Cd^{2+}, Cu^{2+}, Co^{2+}, Ni^{2+}). Measurements were conducted across a concentration range of 10^{-14} to 10^{-4} M. Data points represent mean ± standard deviation ($n = 3$). The concentration-dependent response demonstrates selective metal binding to the EPS bio-recognition layer.

sensor exhibits a well-defined selectivity pattern that is directly driven by the mass loading and viscoelastic changes of the binding layer. The interest of Ni^{2+} induced the highest sensitivity response, giving selectivity coefficients larger than 1.0 when the other metals are taken as a primary target against Ni^{2+}. However, when Ni^{2+} was taken as the primary target ion, the sensor exhibited excellent selectivity with coefficients as low as 0.26 for Pb^{2+} and 0.29 for Hg^{2+}.

In summary, while lead, and to a lesser extent mercury, show the highest initial loss and response gradient, indicating strong early sensitivity, nickel provides the weakest response. Cobalt, cadmium, and copper provide moderate sensitivity to low concentrations, and take longer to saturate and thus may have long ranges for detection but may be less sensitive to low concentrations. Each metal's unique response characteristics make it possible to tailor sensor designs according to the specific detection requirements.

In the acoustic SAW control measurements, the bare SiO_2 device showed no meaningful response to Pb^{2+} in natural seawater. The recorded gain values were irregularly scattered across the entire concentration range, and linear regression indicated a very low calibration slope of 2.0831 dB per decade, accompanied by an extremely poor correlation coefficient of $R^2 = 0.0746$. This behavior suggests that, under the experimental conditions, the unmodified SiO_2 substrate lacks measurable acoustic sensitivity to Pb^{2+}. Therefore, the concentration-dependent acoustic attenuation observed in the EPS-coated SAW sensor can be interpreted as being strictly related to the EPS–metal interaction, rather than resulting from non-specific adsorption on the bare substrate.

Electrochemical detection using square wave voltammetry (SWV) without redox mediator

Square Wave Voltammetry (SWV) experiments were carried out directly in seawater, without the addition of external redox mediators, to assess the electrochemical responses of the six target metal ions (Cu^{2+}, Pb^{2+}, Cd^{2+}, Co^{2+}, Ni^{2+}, Hg^{2+}). Under these conditions, the observed variations in peak current (μA) and

Table 5 Signal loss, saturation behavior, and sensitivity gradients for metal ions in acoustic sensor system. Average of three replicates

Metal ion	Initial signal loss at 10^{-14} M (dB)	Saturation concentration (M)	Saturation signal loss (dB)	Sensitivity gradient (dB per decade)	Linear detection range (M)
Co^{2+}	1.70 ± 0.20	10^{-9}	17.31 ± 2.08	3.12 ± 0.35	10^{-14} to 10^{-9}
Ni^{2+}	0.22 ± 0.03	10^{-12}	3.48 ± 0.42	1.63 ± 0.20	10^{-14} to 10^{-12}
Cd^{2+}	3.60 ± 0.40	10^{-9}	24.14 ± 2.90	4.11 ± 0.49	10^{-14} to 10^{-9}
Hg^{2+}	6.58 ± 0.79	10^{-11}	23.65 ± 2.75	5.69 ± 0.65	10^{-14} to 10^{-11}
Pb^{2+}	12.65 ± 1.49	10^{-12}	25.24 ± 2.95	6.29 ± 0.70	10^{-14} to 10^{-12}
Cu^{2+}	4.41 ± 0.53	10^{-8}	25.30 ± 3.02	3.48 ± 0.35	10^{-14} to 10^{-8}

Table 6 Acoustic selectivity coefficients ($K_{i,j}$) based on Love-wave gradients

Primary ion (i)	Pb^{2+}	Hg^{2+}	Cd^{2+}	Cu^{2+}	Co^{2+}	Ni^{2+}
Pb^{2+}	1.00	1.11	1.53	1.81	2.02	3.86
Hg^{2+}	0.90	1.00	1.38	1.61	1.82	3.49
Cd^{2+}	0.65	0.72	1.00	1.18	1.32	2.52
Cu^{2+}	0.55	0.62	0.85	1.00	1.11	2.13
Co^{2+}	0.50	0.55	0.76	0.90	1.00	1.91
Ni^{2+}	0.26	0.29	0.40	0.47	0.52	1.00

potential (V) are attributed to the inherent redox characteristics of each metal and their selective interactions with the extracellular polymeric substances (EPS) coating the electrode surface.

To evaluate the intrinsic electrochemical response of the substrate and confirm that the detected signals originate exclusively from the EPS functional layer, control measurements were conducted using unmodified bare gold electrodes in natural seawater across the same Pb^{2+} concentration range. The recorded peak currents remained nearly constant at all concentrations, resulting in an extremely low calibration slope of 0.0236 μA per decade and a weak correlation coefficient ($R^2 = 0.1079$). This minimal variation indicates that the bare gold electrode exhibits no significant electrochemical sensitivity to Pb^{2+} under the experimental conditions. Consequently, the pronounced peak-current variations observed for the EPS-coated electrodes can be attributed solely to EPS–metal interactions, rather than to non-specific electrochemical activity of the underlying gold substrate (Fig. 6).

The high current intensities recorded for Cu^{2+} (600 μA), Pb^{2+} (300 μA), Cd^{2+} (330 μA), and Co^{2+} (400 μA) suggest a greater ease of electron transfer between these metal ions and the EPS-modified electrode.

Conversely, the lower currents measured for Ni^{2+} (62 μA) and Hg^{2+} (44 μA) suggest either a weaker interaction with the EPS layer or slower reduction kinetics at the electrode–solution interface. Regarding peak potentials, these reflect the energy required for the electrochemical reduction of the metal ions. The highly negative potentials observed for Cu^{2+} (−1.2 V), Pb^{2+} (−1.0 V and −0.78 V), Cd^{2+} (−0.82 V), and Co^{2+} (−0.5 V) indicate that their reduction requires more energy, which is typical for metals with more negative standard reduction potentials.[55] The presence of multiple peaks for Pb^{2+} suggests the coexistence of several coordination states or chemical species of lead in solution, interacting differently with the EPS matrix.[68] In contrast, the less negative potentials observed for Ni^{2+} (−0.25 V) and Hg^{2+} (−0.05 V) indicate a thermodynamically more favorable reduction under the tested conditions.

Electrochemical parameters derived using the Butler–Volmer framework are detailed in Table 7. This model links peak current intensities (I_p) and potentials (E_p) to electron transfer kinetics and thermodynamics, modulated by EPS preconcentration and seawater's chloride-rich matrix.

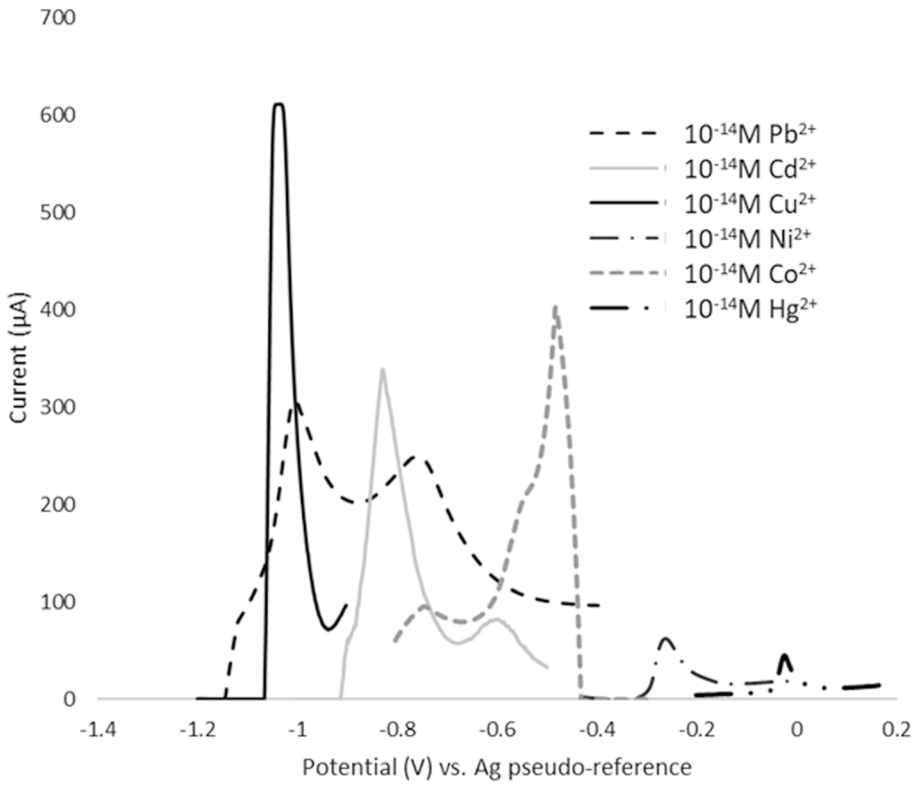

Fig. 6 Square wave voltammograms showing the electrochemical behavior of six metal ions (Pb^{2+}, Hg^{2+}, Cd^{2+}, Cu^{2+}, Co^{2+}, Ni^{2+}) at a fixed concentration of 10^{-14} M in natural seawater without redox mediator. The EPS-functionalized gold electrode demonstrates metal-specific voltammetric signatures. Measurements were performed using SWV with 10 mV amplitude, 10 mV step potential, and 17 Hz frequency.

Table 7 Electrochemical parameters derived using the Butler–Volmer framework for metal ion detection *via* square wave voltammetry (SWV) in natural seawater without redox mediator. Parameters were determined at a metal ion concentration of 10^{-14} M. Values represent mean ± standard deviation ($n = 3$)

Metal ion	Overpotential η (V)	Concentration C (mol cm^{-3})	Diffusion coefficient D (cm^2 s^{-1})	Current density j (A cm^{-2})	Exchange current density j_0 (A cm^{-2})
Cu^{2+}	−0.20	1.12×10^{-6}	4.96×10^{-6}	0.0060	0.00060
Pb^{2+} (peak 1)	−0.10	5.58×10^{-7}	4.99×10^{-6}	0.0030	0.00030
Pb^{2+} (peak 2)	−0.08	5.58×10^{-7}	4.99×10^{-6}	0.0030	0.00030
Cd^{2+}	−0.07	6.14×10^{-7}	5.01×10^{-6}	0.0033	0.00033
Co^{2+}	−0.05	7.44×10^{-7}	5.00×10^{-6}	0.0040	0.00040
Ni^{2+}	−0.05	1.84×10^{-7}	5.00×10^{-6}	0.0010	0.00001
Hg^{2+}	−0.05	1.49×10^{-7}	4.97×10^{-6}	0.0008	0.00008

The overpotentials ($\eta = E_p - E^{o\prime}$), critical for assessing thermodynamic and kinetic barriers, revealed distinct behaviors. Cu's high η (−0.20 V) indicated a significant energy barrier, requiring substantial overpotential to drive reduction despite its high surface concentration (C; 1.12×10^{-6} mol cm^{-3}) and exchange current density (j_0; 0.006 A cm^{-2}), which compensated to yield the highest peak current I_p (600 μA).[85] Pb's η values (−0.10 V for Peak 1, −0.08 V for Peak 2) reflected dual coordination states: Peak 1 (free Pb^{2+}) had a borderline η, suggesting moderate thermodynamic challenge, while Peak 2 would benefit from chloride stabilization ($PbCl_x$), reducing η and facilitating reduction at a less negative E_p (−0.78 V).[85] Cd's η (−0.07 V) was small, indicating favorable thermodynamics and kinetics, supported by strong EPS affinity, resulting in robust I_p (330 μA). Co, Ni, and Hg shared small η (−0.05 V), suggesting thermodynamically facile reductions due to less negative $E^{o\prime}$ values. However, Ni and Hg's low I_p (62 μA and 44 μA) highlighted kinetic limitations, with low C and j_0 reflecting weak EPS interactions or inactive complexes, particularly for Hg, where strong EPS binding may sequester ions.[86]

On the other hand, the diffusion coefficient ($D \sim 5 \times 10^{-6}$ cm^2 s^{-1}) was constant across all metals, indicating uniform ion transport in seawater's high ionic strength, with minor variations ($4.96–5.01 \times 10^{-6}$ cm^2 s^{-1}) potentially due to complexation effects, such as $PbCl_x(2 - x)$ or Hg complexes.[87] The uniform D underscores that transport is not a limiting factor; instead, variations in I_p are driven by C, j_0, and η. Pb's dual peaks, with distinct η, confirm multiple electroactive species, necessitating tailored EPS designs to enhance specificity.[26]

To further examine the sensitivity and responsiveness of the system under realistic conditions, the variation of the peak current was tested across metal ion concentrations ranging from 10^{-14} M to 10^{-2} M (Fig. 7). For most target ions Cu^{2+}, Pb^{2+}, Cd^{2+}, Ni^{2+}, and Hg^{2+}, the peak current exhibited minimal variation (changes <5%) across this wide concentration range.

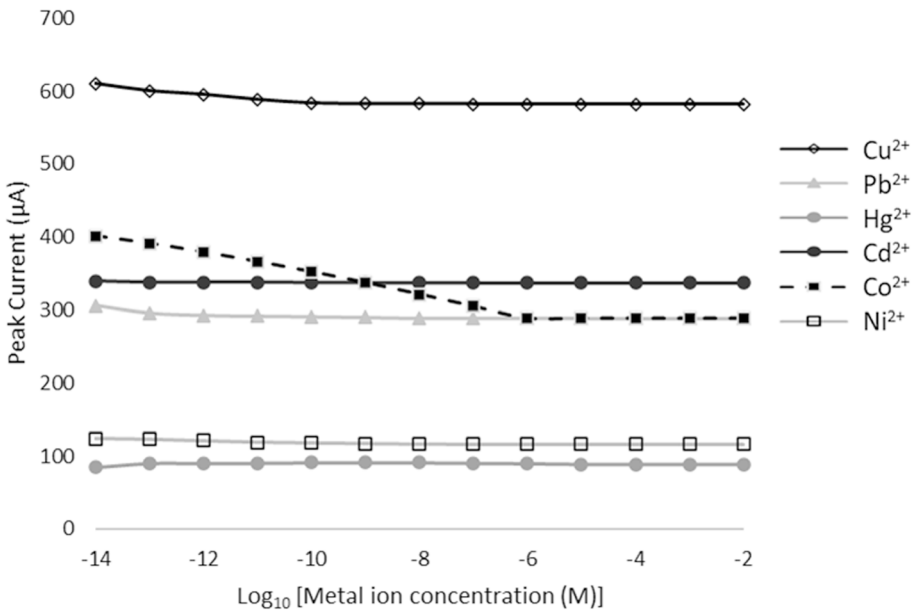

Fig. 7 Square wave voltammetry (SWV) peak current response as a function of metal ion concentration in natural seawater without redox mediator. Six trace metals (Pb^{2+}, Hg^{2+}, Cd^{2+}, Cu^{2+}, Co^{2+}, Ni^{2+}) were tested across a concentration range of 10^{-14} to 10^{-2} M. Data points represent mean ± standard deviation ($n = 3$). The minimal variation in peak current (<5% for most metals) indicates limited direct electrochemical response without a redox mediator, attributed to the high ionic strength of seawater and competitive binding effects.

Cobalt was an exception, showing a relatively more pronounced signal attenuation of up to 28% at higher concentrations.

The limited current variation across this wide concentration range for all tested metals reinforces the conclusion that matrix effects in seawater such as strong complexation by natural ligands, competitive ion interactions, and high ionic strength severely limit the sensitivity of direct SWV measurements. These factors likely mask any proportional relationship between the added metal concentration and the electrochemical response.

However, in comparison, deionized freshwater, under pH conditions that do not allow for effective ionization of metal ions and in the absence of supporting electrolytes, while useful for isolating metal–EPS interactions without interference, inherently limits the measured current due to its very low ionic conductivity. But such conditions fail to represent the complexity of real environmental matrices[55,87] and seawater provides a more relevant testing medium to evaluate the robustness and selectivity of EPS-functionalized electrochemical interfaces. Overall, these findings emphasize the need for sample pre-treatment steps or the introduction of mediators to liberate metals into labile, detectable forms, thereby enhancing detection sensitivity and selectivity.

Electrochemical detection with ferri/ferrocyanide ($[Fe(CN)_6]^{3-/4-}$) redox mediator

The ferri/ferrocyanide ($[Fe(CN)_6]^{3-/4-}$ 10 mM) redox couple was utilized as an external mediator in the electrochemical system with the SPGEs, acting as a reversible electron shuttle. The electrochemical characterization of the EPS-functionalized sensor under these conditions highlights key differences in voltammetric response between seawater and deionized water, summarized in Table 8.

Prior to EPS deposition, SWV measurements revealed a significantly higher peak current for the mediator in seawater (350.3 ± 7.2 μA) compared to deionized freshwater (73.8 ± 2.6 μA). This was accompanied by a slight shift to a lower redox potential in seawater (0.16 V *vs.* 0.19 V). The enhanced current in seawater is attributed to its higher ionic strength and conductivity, which improves charge screening and facilitates faster mass transport of the redox species to the electrode surface.[55,88] Despite the substantial difference in peak current, the integrated charge values remained comparable (205 ± 53 C in seawater *vs.* 194 ± 20 C in freshwater), suggesting a similar quantity of electroactive species participating in the redox process within the measurement timescale.[89] Upon deposition of the EPS layer onto the SPGEs, both peak current and charge decreased in both media. This indicates that the polysaccharide matrix partially hinders electron transfer, likely due to a combination of creating a physical diffusion barrier and potential chemical complexation or interaction with the redox probe itself.[90,91] Notably, while the SWV peak potential remained unchanged in seawater (0.16 V), a clear positive shift was observed in freshwater (to 0.31 V). This suggests that seawater's buffered, high ionic strength environment helps maintain stable interfacial charge transfer conditions, whereas the low ionic strength deionized water is more susceptible to kinetic and capacitive effects introduced by the insulating properties of the EPS layer.[92,93] These comparative findings underscore the importance of the matrix and justify focusing subsequent metal detection studies in seawater.

SWV data for six heavy metal ions Cu^{2+}, Pb^{2+}, Hg^{2+}, Cd^{2+}, Co^{2+}, and Ni^{2+} were analyzed using the $[Fe(CN)_6]^{3-/4-}$ redox couple in seawater to assess their electrochemical signal suppression (ΔI peak) across a concentration range of 10^{-14} M to 10^{-4} M (Fig. 8).

Within this sub-range, lead (Pb) exhibited the highest sensitivity with a slope of 12.76 μA per decade and excellent linearity ($R^2 \approx 0.998$), followed by mercury (Hg) at 12.60 μA per decade ($R^2 \approx 0.996$) and cobalt (Co) at 12.00 μA per decade ($R^2 \approx 0.995$). Nickel (Ni) also showed strong performance with a slope of 11.60 μA per decade and $R^2 \approx 0.994$. Cadmium (Cd) had a moderate slope of 9.25 μA per decade ($R^2 \approx 0.982$), while copper (Cu) displayed the lowest sensitivity at 6.12 μA per decade with the weakest linearity ($R^2 \approx 0.963$), possibly due to less favorable electrode kinetics or weaker interactions at lower concentrations.

The electrochemical behavior of each metal in natural seawater during interaction with the redox probe highlights significant differences between the metals studied. Pb^{2+}, Hg^{2+}, Co^{2+}, and Ni^{2+} would have ideal targets for sensitive detection using EPS-functionalized SWV sensors. Indeed, the highest slopes and the strongest linearity are indicative of an effective inhibition of the charge transfer suggesting a strong complexation or adsorption on the surface of the electrode, probably reinforced by the interaction with the EPS coating. On the contrary, the ability of the Cu^{2+} for quantification is reduced without additional optimization. The lower signal and linearity of the Cu would be indicators of a competitive speciation in seawater, a lower EPS bond or slow redox kinetics.

The distinct sensitivity slopes observed for each metal (Pb^{2+} 12.76 μA per decade, Hg^{2+} 12.60 μA per decade, and Cu^{2+} 6.12 μA

Table 8 Peak current and potential parameters from square wave voltammetry (SWV) measurements in natural seawater and deionized water using $[Fe(CN)_6]^{3-/4-}$ (10 mM) as a redox mediator. Measurements were performed before and after EPS layer deposition. Redox mediator concentration: 10 mM; metal ion concentration range tested: 10^{-14} to 10^{-4} M. Values represent mean ± standard deviation ($n = 3$)

	Natural sea water		Diosmosed freshwater	
	Bare sensor	EPS coated	Bare sensor	EPS coated
I_p (μA)	350.28 ± 7.19	214.79 ± 24.79	73.82 ± 2.6	50.78 ± 7.36
Peak potential (V)	0.16 ± 0.01	0.16 ± 0.01	0.19 ± 0.01	0.31 ± 0.02
Charge (Q)	205.55 ± 17.60	112.10 ± 53.02	193.81 ± 19.79	105.50 ± 16.66

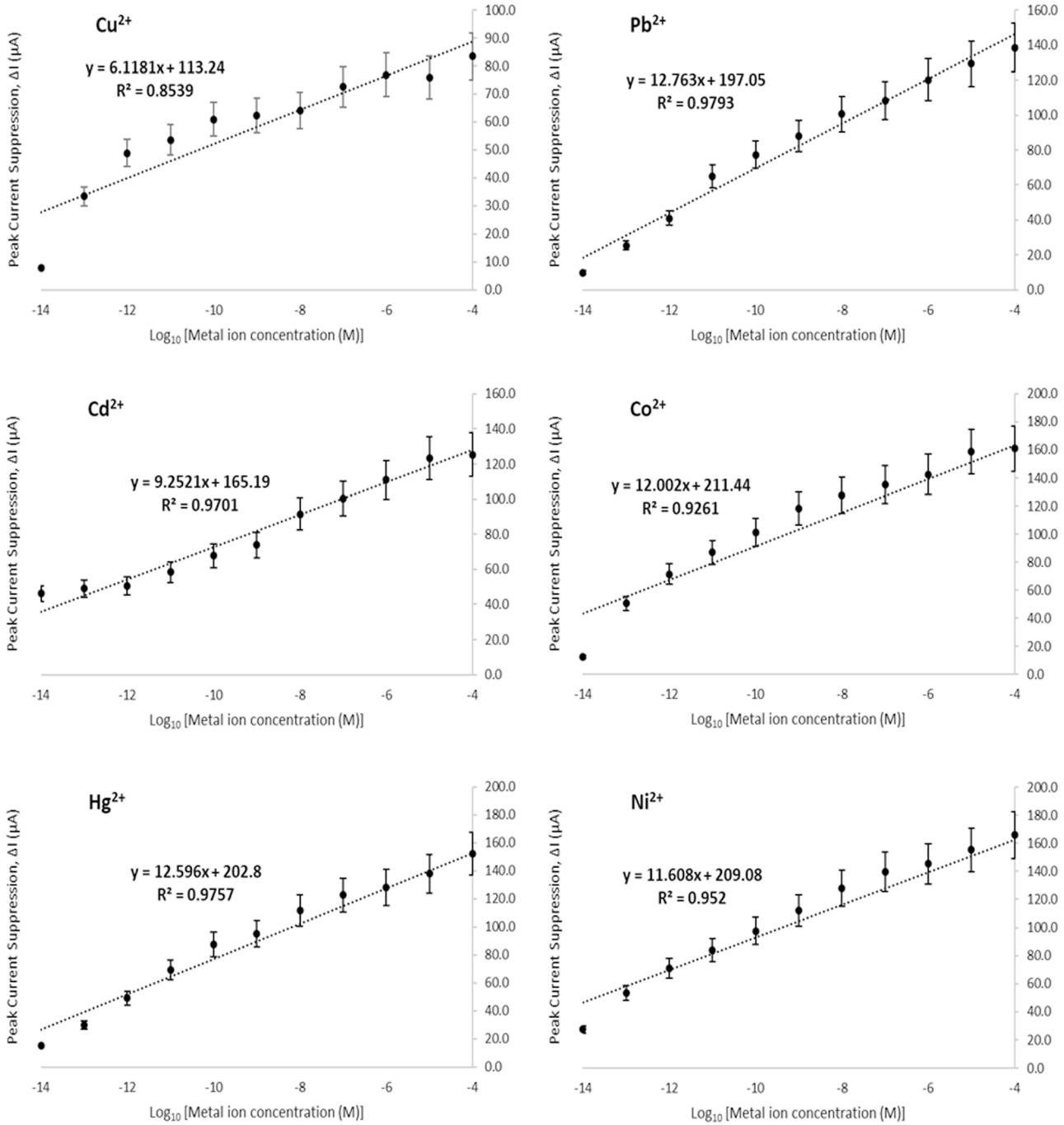

Fig. 8 Square wave voltammetry (SWV) response showing peak current suppression (ΔI) as a function of metal ion concentration in natural seawater using $[Fe(CN)_6]^{3-/4-}$ (10 mM) as a redox mediator. Six trace metals (Pb^{2+}, Hg^{2+}, Cd^{2+}, Cu^{2+}, Co^{2+}, Ni^{2+}) were analyzed across a concentration range of 10^{-14} to 10^{-4} M. Dashed lines represent linear regression fits. Slope values in legends indicate detection sensitivity (μA per decade). Data points represent mean ± standard deviation ($n = 3$). Lead and mercury show the highest sensitivities (12.76 and 12.60 μA per decade, respectively).

per decade) are not merely a result of surface preconcentration; they reflect the selective modulation of the EPS layer's viscoelastic and dielectric properties upon metal binding. Metals that induce the strongest viscoelastic damping and structural rearrangement, as evidenced by the highest acoustic amplitude attenuation gradients (Pb^{2+} 6.29 dB per decade, Hg^{2+} 5.69 dB per decade; Table 5 and Fig. 5), create a more effective diffusion barrier for the $[Fe(CN)_6]^{3-/4-}$ mediator, leading to greater peak-current suppression. Concurrently, metal-specific coordination to polar functional groups (FTIR spectra, Table 1) alters the local dielectric environment, modifying the double-layer capacitance and potential distribution at the electrode–EPS seawater interface. These coupled mechano-dielectric changes directly influence electron transfer kinetics, as shown by the

Butler–Volmer parameters (Table 7) measured without a mediator and in the differential mediator inhibition slopes presented here. Thus, the electrochemical signatures serve as a sensitive, complementary readout of the same selective binding events detected acoustically, reinforcing the multifunctional role of microalgal EPS as a bioinspired recognition layer for marine trace metal sensing.

The Limit of Detection (LOD) achieved in the present study for trace metals in natural seawater, particularly for Pb^{2+} (10^{-12} M) and Hg^{2+} (10^{-11} M),[94] shows very good sensitivity compared with the present regulatory limits and other sophisticated detection methods. WHO and the United States Environmental Protection Agency have established a maximum allowable concentration for lead and mercury in drinking water at 10^{-8} M (10 μg L^{-1}) and 5×10^{-9} M (1 μg L^{-1}), respectively. These LODs are 3–4 orders of magnitude lower than those in this study, indicating the potential of these EPS-functionalized sensors to provide an early warning system for trace metal pollution in marine environments.

Moreover, in relation to other state-of-the-art techniques, such as ICP-MS, which reaches LODs as low as 10^{-12} M for Pb^{2+} and Hg^{2+}, under controlled laboratory conditions,[95] the sensors developed here have shown comparable sensitivity in addition to being low-cost, portable, and suitable for *in situ* applications. Conversely, electrochemical sensors not functionalized by EPS usually have LODs ranging between 10^{-7} and 10^{-6} M, in this way emphasizing the high level of enhancement introduced by the bio-recognition layer provided by EPS.[96] These results confirm the appropriateness of the sensors developed for real-world marine monitoring, where trace metal concentrations are often below regulatory thresholds but still pose ecological risks.

Complementarily to the results of the acoustic technique, selectivity of the electrochemical transduction-mediated SWV was assessed by using the slopes of the calibration curves presented in Fig. 8. The corresponding selectivity coefficients were calculated and are compiled in Table 9.

A coefficient value ($K_{ij} < 1$) indicates that the sensor is more selective toward the primary ion than it is toward the interferent. Contrasted with the acoustic mode, which favored nickel, the electrochemical mode exhibits high selectivity for copper. Shown in Table 9, when Cu^{2+} is the primary ion, the coefficients for all other metals are between 0.48 and 0.66, confirming minimal interference. However, when targeting Pb^{2+}, the presence of Cu^{2+} results in a coefficient of 2.08, indicating competitive binding. In order to illustrate the specific role of the EPS matrix in enhancing heavy metal detection, lead Pb^{2+} was used as a representative analyte.

Table 9 Electrochemical selectivity coefficients ($K_{i,j}$) based on square wave slope

Primary ion (i)	Pb^{2+}	Hg^{2+}	Co^{2+}	NI^{2+}	Cd^{2+}	Cu^{2+}
Pb^{2+}	1.00	1.01	1.06	1.10	1.38	2.08
Hg^{2+}	0.99	1.00	1.05	1.09	1.36	2.06
Co^{2+}	0.94	0.95	1.00	1.03	1.30	1.96
Ni^{2+}	0.91	0.92	0.97	1.00	1.24	1.87
Cd^{2+}	0.72	0.73	0.77	0.80	1.00	1.49
Cu^{2+}	0.48	0.49	0.51	0.53	0.66	1.00

Conclusion

This research presents a significant potential of EPS from microalgae as multifunctional and bioinspired interfaces for the detection of trace metals under real seawater conditions. Using a multimodal spectroscopic, acoustic, and electrochemical approach, the work demonstrates how EPS interacts systematically with six environmentally-relevant metal ions Cu^{2+}, Pb^{2+}, Hg^{2+}, Cd^{2+}, Co^{2+}, and Ni^{2+} *via* different sensing modes. Spectroscopy through Fourier-transform infrared (FTIR) confirmed successful immobilization of EPS on SiO_2- or Au-based surfaces, and provided direct evidence of metal binding, *via* red shifted O–H, C=O, COO^-, and sulfate vibrational modes. These spectral signatures showed a combination of hydrogen bonding, electrostatic attraction, and coordination interactions, which collectively were affected by the physicochemical complexity of seawater. Acoustic sensing using Love wave-based SAW devices showed a robust signal loss upon exposure to trace metals, with reliable detection to low concentrations of 10^{-14} M. Metals with higher electronegativity, like Pb and Hg, presented early-stage sharp signal losses, while Ni and to a lesser extent Co presented with lower and/or delayed signal losses, which should be interpreted as differences in the speciation of metals (*i.e.*, the influence of EPS–metal complexation on acoustics). The noisy signal profile in seawater *versus* in freshwater illustrates the challenges posed by the ionic strength and viscosity of seawater, and competing interactions—but also highlights the relevance of this platform to *in situ* deployment. Electrochemical detection using SWV, both with and without $[Fe(CN)_6]^{3-/4-}$ redox mediator, demonstrated an overall metal-specific redox response unique to the electrochemical detection type, as well as showed evidence of EPS-mediated preconcentration and adsorption of some metals. High peak currents associated with Cu, Pb, and Cd were correlated with good redox response and favorable kinetics of those metal species. Solutions of Hg and Ni were less responsive due to either kinetic limitations or strong binding with EPS. Sensitivity was improved when ferri-/ferrocyanide was used as a mediator, making differentiation between seawater and freshwater matrices possible, as well as validating that externally-supplied redox mediators were still important at high ionic strengths. Overall, results from this work further support that EPS may serve as a solid and selective functional layer for biofouling marine sensors that can integrate to both acoustic and electrochemical systems. Additionally, this work shows that marine matrix effects (ionic strength, natural organic ligands, and metal complexation) can modulate the performance of these sensors. Future plans should include developing hybrid EPS-based sensor platforms that can be used for real-time monitoring, and future bioremediation of trace metals in coastal and estuarine areas. Future work will also focus on ways to better stabilize signals at high saline concentrations, modifying EPS structure and shape for increased metal selectivity, and pre-treatment procedures to overcome the limits of detection regarding promptitude of metal speciation.

Author contributions

Z. M.: conceptualization, investigation, formal analysis, writing – original draft, visualization. J. A.: investigation, methodology, data curation. O. T.: methodology (acoustic sensors), formal analysis, supervision. H. S.: formal analysis, software. M. R.: investigation (acoustic measurements), validation. R. K.: methodology (chemical aspects), supervision, formal analysis, writing – review & editing. J.-L. L.: investigation (acoustic measurements). C. D.: supervision, funding acquisition. H. B. O.: conceptualization, supervision, formal analysis, writing – original draft, visualization. All authors contributed to writing – review & editing and approved the final manuscript.

Conflicts of interest

The authors declare no competing interest.

Data availability

The datasets generated and analyzed during the current study, including raw FTIR spectra, SEM-EDX elemental mappings, Love wave acoustic signals, and square wave voltammetric curves for trace metals in seawater, are available from the corresponding author upon reasonable request. Due to the large file size of the raw datasets, they have not been deposited in a public repository. Requests for data should be directed to the corresponding author at mazouz.zouhour645@gmail.com.

Acknowledgements

This project has received financial support from the CNRS through the MITI interdisciplinary programs through its exploratory research program (project PollutAlert).

References

1 G. I. Edo, P. O. Samuel, G. O. Oloni, G. O. Ezekiel, V. O. Ikpekoro, P. Obasohan, *et al.*, *Chem. Ecol.*, 2024, **40**, 322–349, DOI: 10.1080/02757540.2024.2306839.
2 H. Ali, E. Khan and I. Ilahi, *J. Chem.*, 2019, **2019**, 6730305, DOI: 10.1155/2019/6730305.
3 N. Kolarova and P. Napiórkowski, *Ecohydrol. Hydrobiol.*, 2021, **21**, 655–671, DOI: 10.1016/j.ecohyd.2021.02.002.
4 P. M. Patil, A. R. Matkar, V. B. Patil, R. Gurav and M. J. Dhanavade, in *Modern Approaches in Waste Bioremediation: Environmental Microbiology*, ed. J. Shi, Springer, Cham, 2023, pp. 377–407, DOI: 10.1007/978-3-031-24086-7_18.
5 S. Madhav, A. Ahamad, A. K. Singh, J. Kushawaha, J. S. Chauhan, S. Sharma *et al.*, in *Sensors in Water Pollutants Monitoring: Role of Material*, ed. D. Pooja, P. Kumar, P. Singh and S. Patil, Springer, Singapore, 2020, pp. 43–62, DOI: 10.1007/978-981-15-0671-0_4.
6 F. G. Calvo-Flores, J. Isac-García and J. A. Dobado, *Emerging Pollutants: Origin, Structure, and Properties*, Wiley, Hoboken, NJ, 2018, DOI: 10.1002/9783527691203.
7 O. Dagdag, T. W. Quadri, R. Haldhar, S. C. Kim, W. Daoudi, E. Berdimurodov *et al.*, in *Heavy Metals in the Environment: Management Strategies for Global Pollution, ACS Symposium Series*, American Chemical Society, Washington, DC, 2023, pp. 3–24, DOI: 10.1021/bk-2023-1456.ch001.
8 M. M. Sarkar, M. F. Rohani, M. A. R. Hossain and M. Shahjahan, *Biol. Trace Elem. Res.*, 2022, **200**, 4139–4149, DOI: 10.1007/s12011-021-02692-4.
9 S. Afshan, S. Ali, U. S. Ameen, M. Farid, S. A. Bharwana, F. Hannan, *et al.*, *Res. J. Chem. Environ. Sci.*, 2014, **2**, 74–79.
10 B. Ghose, *Food Energy Secur.*, 2014, **3**, 86–95, DOI: 10.1002/fes3.48.
11 S. Bazsefidpar, C. Saweres-Argüelles, G. Gutiérrez, M. Matos, V. Calero, E. Serrano-Pertierra, *et al.*, *Microchem. J.*, 2024, **205**, 111702, DOI: 10.1016/j.microc.2024.111702.
12 W. Gongi, H. Touzi, H. Sakly, H. Ben Ouada, O. Tamarin and H. Ben Ouada, *J. Polym. Environ.*, 2022, **30**, 4738–4748, DOI: 10.1007/s10924-022-02555-6.
13 W. Gongi, M. Rube, H. Ben Ouada, H. Ben Ouada and O. Tamarin, *Sensors*, 2023, **23**, 803, DOI: 10.3390/s23020803.
14 C. Li, Y. Yu, A. Fang, D. Feng, M. Du, A. Tang, *et al.*, *Lett. Appl. Microbiol.*, 2022, **75**, 1064–1073, DOI: 10.1111/lam.13563.
15 D. Cui, C. Tan, H. Deng, X. Gu, S. Pi, T. Chen and A. Li, *Archaea*, 2020, **2020**, 8891543, DOI: 10.1155/2020/8891543.
16 C. Qu, S. Yang, M. Mortimer, M. Zhang, J. Chen, Y. Wu, *et al.*, *Environ. Pollut.*, 2022, **295**, 118651.
17 M. Danouche, N. El Ghachtouli and H. El Arroussi, *Heliyon*, 2021, **7**, e07347.
18 S. Naveed, C. Li, X. Lu, S. Chen, B. Yin, C. Zhang and Y. Ge, *Crit. Rev. Environ. Sci. Technol.*, 2019, **49**, 1769–1802.
19 M. Vandenbossche, M. Jimenez, M. Casetta and M. Traisnel, *Crit. Rev. Environ. Sci. Technol.*, 2015, **45**, 1644–1704.
20 S. Ethiraj and M. S. Samuel, *Biocatal. Agric. Biotechnol.*, 2024, **58**, 103316.
21 D. Mahlangu, K. Mphahlele, F. De Paola and N. H. Mthombeni, *Water*, 2024, **16**, 718.
22 Z. Yu, B. Chu, L. Meng and N. Xu, *Microchem. J.*, 2025, 115329.
23 A. T. Lombardi and A. A. H. Vieira, *Phycologia*, 1999, **38**, 283–288.
24 A. T. Lombardi, T. M. R. Hidalgo and A. A. H. Vieira, *Chemosphere*, 2005, **60**, 453–459.
25 Q. Xie, N. Liu, D. Lin, R. Qu, Q. Zhou and F. Ge, *Environ. Pollut.*, 2020, **263**, 114102.
26 J. Zhang, F. Zhou, Y. Liu, F. Huang and C. Zhang, *Sci. Total Environ.*, 2020, **704**, 135368.
27 S. Zheng, Q. Zhou, C. Chen, F. Yang, Z. Cai, D. Li, Q. Geng, Y. Feng and H. Wang, *Sci. Total Environ.*, 2019, **660**, 1182–1190.
28 W. Ciempiel, M. Czemierska, M. Szymańska-Chargot, A. Zdunek, D. Wiącek, A. Jarosz-Wilkołazka, *et al.*, *Molecules*, 2022, **27**, 7153.
29 C. Li, P. Li, H. Fu, J. Chen, M. Ye, S. Zhai, *et al.*, *Sci. Total Environ.*, 2023, **871**, 161995.
30 S. Naveed, Q. Yu, C. Zhang and Y. Ge, *Environ. Pollut.*, 2020, **261**, 114233.

31 M. Xie, N. Liu, D. Lin, Q. Zhou and F. Ge, *Aquat. Toxicol.*, 2019, **213**, 105213.
32 R. Helim, A. Zazoua and H. Korri-Youssoufi, *Chemosensors*, 2024, **12**, 267.
33 F. Rejab, N. E. Dardouri, A. Rouis, M. Echabaane, H. Nasri, B. Lakard, *et al.*, *Micromachines*, 2024, **15**, 1508.
34 W. Gongi, K. Mougin, M. Rube, C. Dejous, H. Ben Ouada and O. Tamarin, *Sci. Rep.*, 2025, **15**, 217.
35 X. Li, J. Lu, M. Li, S. Wang, Y. Liu, Q. Zhou and F. Ge, *World J. Microbiol. Biotechnol.*, 2025, **41**, 144.
36 W. Gongi, K. Mougin, M. Rube, C. Dejous, H. Ben Ouada and O. Tamarin, *Sci. Rep.*, 2025, **15**, 21784.
37 A. S. Y. Ting, K. H. Tiew and K. P. Song, *Int. J. Environ. Sci. Technol.*, 2025, **22**, 8883–8894.
38 J. Wu, X. Yue, T. Wang, Y. Zhang, Y. Jin and G. Li, *Colloids Surf., A*, 2025, **717**, 136850.
39 W. Ciempiel, M. Czemierska, D. Wiącek, M. Szymańska, A. Jarosz-Wilkołazka and I. Krzemińska, *Sci. Rep.*, 2025, **15**, 9093.
40 Y. Tang, Y. Li, P. Chen, S. Zhong and Y. Yang, *Bioessays*, 2024, **46**, e2400111.
41 R. Helim, A. Zazoua and H. Korri-Youssoufi, *Chemosensors*, 2024, **12**, 267.
42 H. Zhang, L. Li, C. Wang, Q. Liu, W.-T. Chen, S. Gao and G. Hu, *Nanoscale*, 2025, **17**, 2386–2407.
43 H. Lee, K. Nam, J. W. Yang, J. I. Han and Y. K. Chang, *Algal Res.*, 2016, **14**, 79–82.
44 P. V. Bramhachari and G. P. Nagaraju, in *Marine Pollution and Microbial Remediation*, Springer, 2017, pp. 67–85.
45 V. O. Liemelianov, V. M. Rylyuk and M. I. Skypa, *Geofiz. Zh.*, 2024, **46**, 97–108.
46 K. Sathish, M. Hamdi, R. C. Venkata, M. Alibakhshikenari, M. Ayadi, G. Pau, *et al.*, *Sensors*, 2023, **23**, 5108.
47 M. Le Menn and R. Naïr, *Front. Mar. Sci.*, 2022, **9**, 1031824.
48 P. S. Petrov, A. D. Zakharenko and M. Y. Trofimov, *Acoust. Phys.*, 2012, **58**, 700–707.
49 W. Gongi, H. Ben Ouada and F. Ghozzi, *J. Appl. Phycol.*, 2021, **33**, 1234–1245.
50 H. M. Copeland, S. Maye, G. MacLeod, D. Brabazon, C. Loscher and B. Freeland, *Carbohydr. Polym. Technol. Appl.*, 2025, **10**, 100857.
51 H. Zhang and W. Davison, *Anal. Chem.*, 1995, **67**, 3391–3400.
52 R. M. Town, M. Filella, H. P. van Leeuwen, J. Buffle and K. J. Wilkinson, *Environ. Sci. Technol.*, 2012, **46**, 10487–10494.
53 O. Tamarin, C. Dejous, D. Rebière, J. Pistré, S. Comeau and J. L. Aucouturier, *Biosens. Bioelectron.*, 2003, **18**, 755–763.
54 C. Dejous, H. Hallil, V. Raimbault, D. Rebière and O. Tamarin, *Sensors*, 2016, **16**, 915.
55 A. Choudhari, M. Rube, I. Sadli, M. Sebeloue, O. Tamarin and C. Dejous, *IEEE Sens. J.*, 2024, **24**, 22300–22306.
56 A. J. Bard and L. R. Faulkner, *Electrochemical Methods: Fundamentals and Applications*, Wiley, 2001.
57 V. Mirčeski, Š. Komorsky-Lovrić and M. Lovrić, *Square-Wave Voltammetry: Theory and Application*, Springer, 2007.
58 Z. Chen, S. Wang, Z. Hui, F. Wang, Y. Ye, Y. He, *et al.*, *Front. Sustainable Food Syst.*, 2024, **8**, 1412584.
59 M. Behera, S. Ram and K. Maheshwari, *Int. Nano Lett.*, 2013, **3**, 17.
60 H. Yin, N. Li, Y. Si, H. Zhang, B. Yang and J. Wang, *Nanoscale Horiz.*, 2020, **5**, 1200–1212.
61 A. Omoike and J. Chorover, *Biomacromolecules*, 2004, **5**, 1219–1230.
62 W. Gongi, J. L. G. Pinchetti, N. Cordeiro, S. Sadok and H. Ouada, *Algal Res.*, 2021, **59**, 102453.
63 C. Zhu, X. Su, Y. Tang and L. Wang, *Algal Res.*, 2023, **69**, 103999.
64 S. Ozturk, B. Aslim and Z. Suludere, *Carbohydr. Polym.*, 2014, **99**, 684–689.
65 X.-F. Sun, S.-G. Wang, X.-m. Zhang, J. Chen, X. Li, B. Gao and Y. Ma, *J. Colloid Interface Sci.*, 2009, **336**, 454–459.
66 Q. Xie, N. Liu, D. Lin, R. Qu, Q. Zhou and F. Ge, *Environ. Pollut.*, 2020, **257**, 113547.
67 D. Wei, M. Li, X. Wang, F. Han, L. Li, J. Guo, L. Ai, L. Fang, L. Liu, B. Du and Q. Wei, *J. Hazard. Mater.*, 2016, **301**, 407–415.
68 A. Venugopal, R. Kas, K. Hau and W. A. Smith, *J. Am. Chem. Soc.*, 2021, **143**, 18581–18591.
69 X. Zhang, N. Xie, Y. Guo, D. Niu, H. Sun and Y. Yang, *J. Hazard. Mater.*, 2021, **418**, 126345.
70 X. Liu, M. Wu, C. Li, Y. Yu, P. Feng, S. Li, Y. Zhang and Q. Zhang, *Molecules*, 2022, **27**, 2407.
71 W. Babiak and I. Krzemińska, *Energies*, 2021, **14**, 4007.
72 S. B. Shah, in *Heavy Metals in Scleractinian Corals*, SpringerBriefs in Earth Sciences, 2021, pp. 1–24.
73 B. P. Frank and G. Belfort, *Langmuir*, 1997, **13**, 6234–6240.
74 H. C. Flemming and J. Wingender, *Nat. Rev. Microbiol.*, 2010, **8**, 623–633.
75 J. Barthel, M. Cattaneo, B. G. Mendis, S. D. Findlay and L. J. Allen, *Phys. Rev. B*, 2020, **101**, 184109.
76 Z. A. Al Disi, D. O. Mohamed, M. A. Al-Ghouti and N. Zouari, *Environ. Technol. Innovation*, 2024, **33**, 103477.
77 Y. Wu, Z. Li, Y. Yang, D. Purchase, Y. Lu and Z. Dai, *Biomolecules*, 2021, **11**, 1715.
78 A. Lasheras, P. G. Saiz, J. Gutiérrez and A. C. Lopes, *Smart Mater. Struct.*, 2020, **29**, 085013.
79 C. M. G. Van den Berg, in *Chemical Processes in Marine Environments*, Springer, 2000, pp. 139–156.
80 W. Moses, J. Bowles, R. Lucke and M. Corson, *Opt. Express*, 2012, **20**, 2082–2098.
81 D. Jorge, C. Barbosa, L. Carvalho, A. G. Affonso, F. Lobo and E. Novo, *Remote Sens.*, 2017, **9**, 460.
82 R. Kudela, S. Hooker, L. Guild, H. Houskeeper and N. Taylor, *Remote Sens.*, 2024, **16**, 192.
83 V. Egorov, E. Zdrachek and V. Nazarov, *Anal. Chem.*, 2014, **86**, 3693–3696.
84 E. Bakker, E. Pretsch and P. Bühlmann, *Anal. Chem.*, 2000, **72**, 1127–1133.
85 A. Smirnov, V. Anisimkin, N. Voronova, E. Shamsutdinova, P. Li, H. Ezzin, *et al.*, *Sensors*, 2022, **22**, 7231.
86 H. Zhang, Y. Yuan, Y. Sun, J. Niu and S. Wang, *Environ. Sci. Technol.*, 2020, **54**, 2717–2725.
87 G. Guibaud, N. Tixier, A. Bouju and M. Baudu, *Chemosphere*, 2003, **52**, 1701–1710.

88 Y. Li, J. Wang and W. Zhang, *Environ. Sci. Technol.*, 2021, **55**, 1234–1245.
89 A. Manivannan, M. S. Seehra and A. Fujishima, *Electrochim. Acta*, 2007, **52**, 4700–4707.
90 R. G. Compton and C. E. Banks, *Understanding Voltammetry*, World Scientific, 2011.
91 G. P. Sheng, H. Q. Yu and X. Y. Li, *Biotechnol. Adv.*, 2010, **28**, 882–894.
92 P. Gupta, V. Kumar and P. Maheshwari, *Sens. Actuators, B*, 2019, **286**, 228–238.
93 C. G. Zoski, *Handbook of Electrochemistry*, Elsevier, 2007.
94 World Health Organization, Guidelines for Drinking-water Quality, 2017, 4th edn, United States Environmental Protection Agency, National Primary Drinking Water Regulations, EPA 816-F-09-004, 2009.
95 S. E. Bahinting, A. P. Rollon, S. Garcia-Segura, V. C. C. Garcia, B. M. B. Ensano, R. R. M. Abarca, J. Yee and M. D. de Luna, *Sensors*, 2021, **21**, 1–18.
96 J. Lazar, C. Schnelting, E. Slavcheva and U. Schnakenberg, *Anal. Chem.*, 2016, **88**, 6821–6827.